electronics

MDPI

Article

Probabilistic and State-Space Modeling of Autonomic Nervous System Dynamics from HRV Signals: A Complementary Probabilistic Framework for Sympathetic–Parasympathetic Characterization

Emi Yuda [1,2]

[1] Innovation Center for Semiconductor and Digital Future (ICSDF), Mie University, 1577 Kurimamachiya-cho, Tsu 514-0102, Mie, Japan; yuda@icsdf.mie-u.ac.jp
[2] Department of Management Science and Technology, Graduate School of Engineering, Tohoku University, 6-6 Aza Aoba, Aramaki, Aoba-ku, Sendai 980-8579, Miyagi, Japan

Abstract

Heart rate variability (HRV) reflects autonomic nervous system (ANS) regulation through beat-to-beat fluctuations in cardiac RR intervals. Conventional HRV analysis relies on deterministic features such as SDNN, RMSSD, HF power, and LF/HF ratio, which quantify autonomic activity but do not model the underlying sympathetic–parasympathetic dynamics. This study proposes a complementary probabilistic framework that treats HRV as the observable output of a latent ANS dynamical system. A linear state-space model with Kalman filtering estimates HRV-derived latent states, interpretable as proxies for sympathetic–parasympathetic balance under predefined physiological assumptions; an Ornstein–Uhlenbeck stochastic differential equation (OU-SDE) captures HRV variability and autonomic recovery; and a Hidden Markov Model (HMM) represents discrete autonomic regime transitions. Applied to ambulatory Holter electrocardiography (ECG) recordings from n = 20 healthy adults, the framework yields interpretable parameters—OU recovery rate $\theta = 0.533 \pm 0.624\ s^{-1}$, diffusion $\sigma = 82.6.2 \pm 105.6\ ms{\cdot}s^{-1/2}$—and confirms the algebraic self-consistency of the OU MLE ($SDNN^2 \approx \sigma^2/(2\theta)$, r = 0.998; note: tautological by construction—both sides derive from the same RR series—and should not be interpreted as independent physiological validation). Each component addresses a distinct aspect of ANS dynamics—continuous-state trajectories, stochastic amplitude, and discrete-regime transitions—and together, they provide complementary layers of autonomic information. This formulation provides uncertainty-aware autonomic assessment suitable for wearable sensing and physiological computing. Note on generalizability: the framework was validated on N = 20 healthy ambulatory adults; findings should not be extrapolated to clinical populations, older cohorts, or individuals with cardiovascular or autonomic pathology without replication in larger, more diverse samples.

Keywords: heart rate variability; autonomic nervous system; state-space model; Kalman filter; stochastic differential equation; Ornstein–Uhlenbeck process; hidden Markov model; sympathetic; parasympathetic; wearable sensing

Check for updates

Academic Editors: Gianluca Rho and Enzo Pasquale Scilingo

Received: 29 September 2026
Revised: 22 October 2026
Accepted: 26 October 2026
Published: 30 October 2026

Copyright: © 2026 by the author. Licensee MDPI, Basel, Switzerland. This article is an open access article distributed under the terms and conditions of the Creative Commons Attribution (CC BY) license.

1. Introduction

The autonomic nervous system (ANS) maintains cardiovascular homeostasis through a continuous interplay of sympathetic (SNS) and parasympathetic (PNS) branches [1]. Beat-to-beat fluctuations in RR intervals—heart rate variability (HRV)—provide a non-invasive

window onto this dual-branch regulation that has been extensively standardized [2,3] and validated across diverse physiological and clinical contexts [4]. Decades of research have established HRV as a reliable biomarker differentiating autonomic profiles in athletes [5], quantifying sex-related differences in vagal tone [6], tracking autonomic dysfunction in cardiac patients [7], and identifying occupational or cognitive stress [8]. This breadth of application makes HRV one of the most widely adopted physiological indices in both clinical practice and wearable health monitoring.

Standard HRV analysis computes time-domain statistics—SDNN (total autonomic variability), RMSSD (short-term vagal activity), and pNN50—alongside frequency-domain metrics: low-frequency (LF, 0.04–0.15 Hz) power, high-frequency (HF, 0.15–0.40 Hz) power, and LF/HF ratio [9,10]. HF power tracks respiratory sinus arrhythmia (RSA) driven by vagal outflow [11], while LF/HF is widely used as a sympatho-vagal balance index [4,10]. Normative reference values have been established as a function of age [12,13], sex [6], recording duration [14], and measurement device [15]. In practice, accurate HRV computation requires careful artifact filtering and RR outlier correction, particularly in ambulatory recordings where motion artifacts are common [16,17].

Despite widespread adoption, conventional HRV analysis is fundamentally limited by treating the autonomic state as static within a fixed epoch. This discards the temporal dynamics of sympatho-vagal regulation, which unfolds continuously over multiple time scales—from respiratory cycles (~4 s) to thermoregulatory rhythms (~30 s) to circadian variation. Moreover, the stochasticity of cardiac regulation arising from neurobiological noise, nonlinear feedback, and respiratory coupling is absorbed into summary statistics rather than explicitly modeled. Nonlinear and multifractal HRV methods partially address this limitation by quantifying signal irregularity [18,19], but they yield empirical complexity measures rather than mechanistic parameters such as relaxation rates, noise intensities, or state transition probabilities. This motivates a shift from descriptive HRV analysis to mechanistic dynamical modeling. No single mathematical framework captures all relevant ANS dynamics simultaneously: Kalman filtering tracks continuous latent states but cannot represent discrete autonomic regimes; OU-SDEs characterize stochastic amplitude in a form linked to classical HRV metrics but do not model regime transitions; and HMMs represent discrete-regime shifts but do not track continuous within-regime dynamics. A complementary multi-scale integration is therefore required.

From an engineering perspective, the ANS is naturally modeled as a dynamical system with latent states (sympathetic and parasympathetic tone) and noisy, multi-dimensional observable outputs (HRV features). This framing calls for state-space estimation and probabilistic inference. Linear Kalman filtering [20] provides principled recursive latent state estimation from noisy observations and has been applied to heartbeat interval sequences through point-process models that track instantaneous heart rate statistics at the level of individual inter-beat intervals [21–23]. State-space models have also been applied to brain dynamics from EEG [24], multi-dimensional digital phenotyping [25], and individualized survival prediction from longitudinal physiological data [26]—demonstrating the generality of the Bayesian filtering framework across biomedical signals.

Stochastic differential equations (SDEs) provide a complementary continuous-time probabilistic language for biological dynamics subject to intrinsic noise [27]. The Ornstein–Uhlenbeck (OU) process [28]—a mean-reverting SDE parameterized by recovery rate θ, equilibrium μ, and noise intensity σ—is the canonical model for homeostatic fluctuations and has been applied to synthetic ECG generation [29] and HRV spectral modeling [30]. Maximum likelihood estimation (MLE) for OU models yields statistically consistent parameter estimates that connect directly to HRV statistics: the stationary variance $\sigma^{2/(2\theta)}$ equals SDNN^2, providing an analytic bridge between stochastic parameters and

classical metrics. Parameter identifiability in the SDE models of biological systems is a key concern [31], and the gray-box MLE approach employed here addresses this by using exact Gaussian transition densities rather than numerical simulation [32].

Hidden Markov Models (HMMs) [33] encode stochastic transitions between discrete latent regimes and are the standard framework for segmenting time series into qualitatively distinct states. HMMs have been applied to physiological signals including electroencephalography (EEG) sleep-staging [34], apnea–bradycardia detection in neonates [35,36], dynamic brain-state analysis from simultaneous intracranial EEG (iEEG) and magnetoencephalography (MEG) recordings [37], and eye movement classification [38]. Recent extensions to physiological stress monitoring include Markov Transition Field representations of electrodermal activity [39] and uncertainty-aware heart rate estimation via belief propagation [40]. These applications demonstrate that discrete-state Markov models capture autonomic regime structure that continuous-state models cannot represent.

Related Work

The mechanistic dynamical modeling of HRV has been pursued along several parallel tracks. Point-process models of heartbeat intervals embed inter-beat intervals into a marked point-process framework with history-dependent inverse-Gaussian distributions updated beat-to-beat via Bayesian filtering [21–23]. State-space methods with Kalman smoothing have been applied to EEG [24] and to mixed digital-phenotyping records [25], demonstrating the generality of latent state inference over noisy biomedical time series. OU-SDEs have been used to characterize long-range correlations in RR intervals [18] and to model mean-reverting autonomic dynamics [28]. HMM segmentation has been applied to apnea detection [35,36] and brain-state dynamics [37]. The present study fills the gap of integrating Kalman filtering, OU-SDE, and HMM into a unified, complementary framework specifically designed for ambulatory HRV.

The present study addresses the gap between descriptive HRV analysis and mechanistic ANS modeling by proposing a hybrid probabilistic–dynamical framework. The framework integrates: (i) a linear time-invariant (LTI) state-space model with Kalman filtering for continuous latent state tracking (HRV-derived proxies for sympathetic–parasympathetic balance under predefined structural constraints); (ii) a conceptual coupled ODE model representing physiological relaxation and reciprocal inhibition (included as a mechanistic interpretive framework; parameters were not estimated from data in this study); (iii) an OU-SDE capturing HRV stochastic fluctuations at the beat-to-beat level; and (iv) a Gaussian HMM characterizing discrete autonomic regime transitions. Rather than treating these as competing alternatives, the framework combines them as complementary parallel components: the Kalman filter provides continuous-state posterior estimates, the OU-SDE supplies their stochastic characterization, and the HMM provides coarser discrete-regime labels for actionable classification. The approach is validated on 20 ambulatory Holter recordings, and model quality is assessed per component via reconstruction RMSE and within-class Bayesian Information Criterion (BIC; e.g., HMM state count). The result is a principled, real-time-capable, and interpretation-friendly framework for autonomic assessment from HRV signals, with direct relevance to wearable sensing [8], biofeedback [41], and clinical autonomic phenotyping [42].

2. Materials and Methods

Section 2 presents the proposed multi-scale ANS monitoring framework before its experimental instantiation. Sections 2.1–2.5 introduce the five theoretical components: the LTI state-space model (Section 2.1), Kalman filter EM for latent-state estimation (Section 2.2), a conceptual ODE mechanistic background motivating the coupling structure (Section 2.3),

the OU-SDE for beat-to-beat stochastic characterization (Section 2.4), and a Hidden Markov Model for discrete autonomic regime segmentation (Section 2.5). Section 2.6 then describes the experimental validation context: participant cohort, data acquisition using wearable ECG sensors (Cardy 303 pico, Suzuken Co., Ltd., Nagoya, Aichi, Japan), and HRV feature extraction (Sections 2.6.1 and 2.6.2). Sections 2.7 and 2.8 cover model evaluation and statistical methods. All signal processing, mathematical modeling, and statistical analyses were performed using Python version 3.11 (Python Software Foundation, Wilmington, DE, USA)/MATLAB R2024a (MathWorks, Natick, MA, USA)]. The three quantitative components (Kalman, OU-SDE, HMM) are fitted independently, and their complementarity is analyzed in Section 3.5.

2.1. Linear Time-Invariant State-Space Model

2.1.1. Rationale and Model Hierarchy

The proposed framework treats ANS dynamics at three levels of abstraction: (a) a continuous-time LTI model capturing the physiological interaction between SNS and PNS; (b) its discrete-time Kalman filter implementation for epoch-by-epoch latent state estimation; (c) an OU-SDE characterizing beat-to-beat stochastic fluctuations within each epoch; and (d) an HMM segmenting the recording into discrete autonomic regimes. Each layer adds complementary information: the LTI/Kalman layer provides continuous posterior state estimates with uncertainty; the OU layer provides stochastic parameters linked to classical HRV metrics; and the HMM layer provides discrete-regime labels suitable for rule-based decision systems. The LTI approximation holds within each 64 s epoch on two grounds. Physiologically, autonomic time constants (SNS efferent: $\tau \approx 15$–30 s; cardiac PNS: $\tau \approx 0.5$–2 s [20,21]) ensure that sympatho-vagal tone shifts negligibly within a single window, so the system operates near a quasi-static equilibrium. Mathematically, a first-order Taylor expansion of the nonlinear ANS vector field $f(x)$ about the epoch mean $\bar{x}$ yields $\dot{x} \approx A(x - \bar{x}) + O(\|x - \bar{x}\|^2)$, where $A = \partial f/\partial x|_{x = \bar{x}}$; for the small intra-epoch state excursions typical of resting ambulatory recordings, the quadratic residual is negligible, justifying the linear representation. The Kalman smoother further absorbs any residual non-stationarity through adaptive innovation covariance. The physiological motivation for the sign pattern of coupling matrix A is developed in the Conceptual Mechanistic Background section below. Acknowledged limitations of the LTI assumption are detailed in Section 4.4.

2.1.2. Latent State Definition and State Equations

Sympathetic (S_k) and parasympathetic (P_k) activity are modeled as a two-dimensional latent state $\mathbf{x}_k = [S_k,\ P_k]^\top$. The discrete-time state equation is:

$$\mathbf{x}_{k+1} = \mathbf{A}_d\,\mathbf{x}_k + \mathbf{B}_d\,\mathbf{u}_k + \mathbf{w}_k, \qquad \mathbf{w}_k \sim \mathcal{N}(\mathbf{0},\,\mathbf{Q})$$

where $\mathbf{A}_d = e^{A\Delta t}$ (zero-order-hold discretization, Δt = epoch duration); $\mathbf{u}_k$ is the exogenous input (e.g., respiratory rate index); and $\mathbf{Q} = \mathrm{diag}(\sigma_S^2, \sigma_P^2)$. The continuous-time system matrix encodes physiological relaxation and interaction:

$$A = \begin{bmatrix} -\alpha_s & \kappa_{sp} \\ \kappa_{ps} & -\alpha_p \end{bmatrix}, \qquad B = \begin{bmatrix} b_s \\ b_p \end{bmatrix}$$

where $\alpha_s, \alpha_p > 0$ are SNS and PNS relaxation rates, and κ_{sp}, κ_{ps} are signed cross-coupling coefficients. Physiologically, $\alpha_p > \alpha_s$ because vagal modulation operates on time constants of 0.3–1 s while sympathetic responses unfold over 5–30 s [4,11].

2.1.3. Observation Equation

The observation vector $\mathbf{y}_k \in \mathbb{R}^4$ is linked to the latent state through:

$$\mathbf{y}_k = \mathbf{C}\mathbf{x}_k + \mathbf{v}_k, \qquad \mathbf{v}_k \sim \mathcal{N}(\mathbf{0}, \mathbf{R})$$

where $\mathbf{R} = \mathrm{diag}\left(\sigma^2_{\mathrm{SDNN}}, \sigma^2_{\mathrm{RMSSD}}, \sigma^2_{HF}, \sigma^2_{\mathrm{LF/HF}}\right)$. The observation matrix $\mathbf{C} \in \mathbb{R}^{4\times 2}$ is structured according to physiological associations:

$$\mathbf{C} = \begin{bmatrix} c_{11} & c_{12} \\ 0 & c_{22} \\ 0 & c_{32} \\ c_{41} & 0 \end{bmatrix}$$

Row 1: SDNN reflects total autonomic drive ($c_{11}, c_{12} > 0$); Row 2: RMSSD reflects PNS only ($c_{22} > 0$); Row 3: HF power reflects vagal RSA only ($c_{32} > 0$); Row 4: LF/HF reflects SNS dominance only ($c_{41} > 0$).

2.2. Kalman Filtering for Latent State Estimation

The Kalman filter recursively computes the posterior mean $\hat{\mathbf{x}}_{k|k}$ and covariance $\mathbf{P}_{k|k}$.
Prediction step:

$$\hat{\mathbf{x}}_{k|k-1} = \mathbf{A}_d\,\hat{\mathbf{x}}_{k-1|k-1} + \mathbf{B}_d\,\mathbf{u}_{k-1}, \qquad \mathbf{P}_{k|k-1} = \mathbf{A}_d\,\mathbf{P}_{k-1|k-1}\,\mathbf{A}_d^\top + \mathbf{Q}$$

Kalman gain and update:

$$\mathbf{K}_k = \mathbf{P}_{k|k-1}\,\mathbf{C}^\top\left(\mathbf{C}\,\mathbf{P}_{k|k-1}\,\mathbf{C}^\top + \mathbf{R}\right)^{-1}$$

$$\hat{\mathbf{x}}_{k|k} = \hat{\mathbf{x}}_{k|k-1} + \mathbf{K}_k\left(\mathbf{y}_k - \mathbf{C}\,\hat{\mathbf{x}}_{k|k-1}\right), \qquad \mathbf{P}_{k|k} = (\mathbf{I} - \mathbf{K}_k\,\mathbf{C})\,\mathbf{P}_{k|k-1}$$

Parameter estimation. System parameters ($\mathbf{A}_d, \mathbf{B}_d, \mathbf{C}, \mathbf{Q}, \mathbf{R}$) were initialized from physiological priors ($\alpha_s = 0.05\ \mathrm{s}^{-1}$, $\alpha_p = 0.5\ \mathrm{s}^{-1}$; $c_{22}, c_{32} = 1$; $c_{41} = -1$; $Q = R = 0.1\,\mathbf{I}$) and refined by Expectation–Maximization [43] using the Kalman smoother in the E-step and coordinate-ascent updates in the M-step. Convergence was declared when the relative change in the complete-data log-likelihood fell below 10^{-6} for 5 consecutive iterations. The inequality constraint $\alpha_p > \alpha_s$ was enforced after each M-step by projecting the updated A matrix onto the physiologically admissible set.

2.3. Conceptual Mechanistic Background: ODE Models of Sympatho-Vagal Interaction [Not Fitted to Data]

The coupled ODE system in Section 2.3.2 directly motivates the sign constraints on the Kalman filter observation matrix C (Section 2.3.3): the inhibitory cross-coupling terms (SNS → PNS and PNS → SNS) correspond to the off-diagonal elements of C, grounding the LTI state-space model in established autonomic physiology. This section provides interpretive context only; no ODE parameters were estimated from data.

2.3.1. Uncoupled First-Order ODEs

SNS and PNS dynamics can first be modeled as independent relaxation systems:

$$\frac{dS(t)}{dt} = -\alpha\,S(t) + k_1\,u(t), \qquad \frac{dP(t)}{dt} = -\beta\,P(t) + k_2\,r(t)$$

where $u(t)$ is stress-related excitation, $r(t)$ is respiratory input encoding RSA, and $\beta > \alpha$ (faster vagal kinetics).

2.3.2. Coupled Nonlinear ODEs with Reciprocal Inhibition

The full model adds mutual inhibition between branches:

$$\frac{dS(t)}{dt} = -\alpha_s\, S(t) - \gamma_{SP}\, P(t)\, S(t) + k_1\, u(t)$$

$$\frac{dP(t)}{dt} = -\alpha_p\, P(t) - \gamma_{PS}\, S(t)\, P(t) + k_2\, r(t)$$

where $\gamma_{SP}, \gamma_{PS} \geq 0$ are cross-inhibition coefficients. The RR interval output is:

$$\mathrm{RR}(t) = \mathrm{RR}_0 - k_s\, S(t) + k_p\, P(t)$$

with $k_s, k_p > 0$ reflecting SNS-mediated acceleration and PNS-mediated deceleration, respectively [4].

2.3.3. Connection to the LTI State-Space Framework

The coupled ODE model above directly motivates the sign structure of the Kalman filter observation matrix C (Section 2.1.3). The inhibitory cross-coupling in Section 2.3.2 implies that: (i) SDNN reflects combined SNS and PNS drive (Row 1 of C sums both contributions); (ii) RMSSD is dominated by PNS activity (Row 2 loads exclusively on the PNS state); and (iii) the LF/HF ratio encodes sympatho-vagal imbalance (Row 3 assigns opposite signs to SNS and PNS). These sign constraints, derived from the physiological ODE structure, are imposed as hard constraints during Kalman EM estimation, grounding the linear state-space model in established autonomic physiology.

2.4. Ornstein–Uhlenbeck SDE Model of HRV Fluctuations

2.4.1. OU Process Formulation and Unit Analysis

Beat-to-beat RR fluctuations driven by ANS noise are modeled as an OU process:

$$dX_t = \theta\,(\mu - X_t)\,dt + \sigma\, dW_t$$

where X_t is the RR interval in ms, $\theta > 0$ is the mean-reversion (homeostatic recovery) rate in s^{-1}, μ is the equilibrium RR interval in ms, $\sigma > 0$ is the diffusion coefficient in $\mathrm{ms}{\cdot}\mathrm{s}^{-1/2}$, and W_t is a standard Wiener process. The unit of σ follows from the SDE: $[dX_t] = \mathrm{ms}$ must equal $[\sigma\, dW_t] = [\sigma]\sqrt{\mathrm{s}}$, giving $[\sigma] = \mathrm{ms} \cdot \mathrm{s}^{-1/2}$. The stationary variance $\mathrm{Var}[X] = \sigma^2/(2\theta)$ has units $(\mathrm{ms})^2 \cdot \mathrm{s}^{-1}/\left(2\,\mathrm{s}^{-1}\right) = (\mathrm{ms})^2$, consistent with SDNN^2. For the two-branch model, separate OU processes are formulated for sympathetic (X_{sym}) and parasympathetic (X_{para}) channels with individual parameters $\left(\theta_{\mathrm{sym}}, \sigma_{\mathrm{sym}}\right)$ and $\left(\theta_{\mathrm{para}}, \sigma_{\mathrm{para}}\right)$.

2.4.2. Discrete-Time Transition Density

The exact conditional distribution over sampling interval Δt is:

$$X_{k+1} \mid X_k \sim \mathcal{N}\left(\mu_{\mathrm{eff},k},\ \sigma^2_{\mathrm{eff}}\right)$$

$$\mu_{\mathrm{eff},k} = \mu + (X_k - \mu)\, e^{-\theta \Delta t}, \qquad \sigma^2_{\mathrm{eff}} = \frac{\sigma^2}{2\theta}\left(1 - e^{-2\theta \Delta t}\right)$$

2.4.3. Maximum Likelihood Estimation

The OU parameters $\boldsymbol{\psi} = [\theta,\ \mu,\ \sigma]^\top$ are estimated by maximizing the exact Gaussian log-likelihood:

$$\ln L(\boldsymbol{\psi}) = -\frac{N}{2}\ln(2\pi) - \frac{1}{2}\sum_{k=1}^{N} \ln \sigma^2_{\mathrm{eff}} - \sum_{k=1}^{N} \frac{\left(X_k - \mu_{\mathrm{eff},k-1}\right)^2}{2\,\sigma^2_{\mathrm{eff}}}$$

Optimization was performed by Nelder–Mead simplex with 10 random initializations (uniform on $\theta \in [10^{-3}, 5]$, $\sigma \in [1, 500]$) to avoid local optima; the solution with the highest $\ln L$ was retained. If Nelder–Mead failed to converge, an ordinary least squares (OLS) closed-form estimate was used as a fallback [32].

2.5. Hidden Markov Model for Autonomic Regime Transitions

Discrete autonomic regimes are modeled as a $K = 3$-state Gaussian HMM with hidden states $q_k \in \{1, 2, 3\}$ representing three autonomic states ordered by decreasing mean RRI (State 1 (High-RRI), State 2 (Intermediate-RRI), State 3 (Low-RRI)). For readability, these states are hereafter referred to as Parasympathetic-Dominant (PD), Balanced (B), and Sympathetic-Dominant (SD), respectively; these are post hoc interpretive labels assigned by RRI rank order and do not constitute direct measurement of sympathetic or parasympathetic nerve activity. Without concurrent MSNA recordings or controlled stress protocols, these designations represent inferred, not confirmed, sympatho-vagal classifications.

2.5.1. Model Parameters

Initial distribution: $\boldsymbol{\pi} = [\pi_1, \pi_2, \pi_3]$, $\pi_i = P(q_1 = i)$.

Transition matrix:

$$\mathbf{A}_{HMM} = \left(a_{ij}\right), \quad a_{ij} = P(q_{k+1} = j \mid q_k = i), \quad \sum_j a_{ij} = 1$$

Gaussian emission distribution for state i:

$$p(\mathbf{y}_k \mid q_k = i) = \mathcal{N}\left(\mathbf{y}_k \,\middle|\, \boldsymbol{\mu}_i, \boldsymbol{\Sigma}_i\right)$$

2.5.2. Baum–Welch Algorithm and Viterbi Decoding

The forward variable $\alpha_k(i) = P\left(\mathbf{y}_{1:k}, q_k = i\right)$ and backward variable $\beta_k(i) = P\left(\mathbf{y}_{k+1:N} \mid q_k = i\right)$ satisfy:

$$\alpha_k(j) = \left[\sum_i \alpha_{k-1}(i)\, a_{ij}\right] \mathcal{N}\left(\mathbf{y}_k \mid \boldsymbol{\mu}_j, \boldsymbol{\Sigma}_j\right), \qquad \beta_k(i) = \sum_j a_{ij}\, \mathcal{N}\left(\mathbf{y}_{k+1} \mid \boldsymbol{\mu}_j, \boldsymbol{\Sigma}_j\right) \beta_{k+1}(j)$$

Parameters $\boldsymbol{\lambda} = \{\boldsymbol{\pi}, \mathbf{A}_{HMM}, \boldsymbol{\mu}_i, \boldsymbol{\Sigma}_i\}$ were optimized by the Baum–Welch EM algorithm [44]. The Viterbi algorithm [45] decoded the most probable state sequence $\hat{q}_{1:N}$.

2.6. Experimental Validation

2.6.1. Participants and Data Acquisition

Twenty healthy adult participants were enrolled in this study. All participants were free of known cardiovascular, neurological, or respiratory disorders. Written informed consent was obtained from all participants prior to enrollment.

Electrocardiographic (ECG) signals were recorded using a SUZUKEN Holter ECG device (Suzuken Co., Ltd., Nagoya, Japan) with a three-lead configuration. Participants underwent ambulatory monitoring under naturalistic daily-life conditions without imposed experimental tasks. QRS complexes and beat labels (Normal [N], Ventricular [V], Supraventricular [S], Artifact [X], and Invalid [NG]) were obtained using the Cardy Analyzer 05 software (Suzuken Co., Ltd., Nagoya, Japan). No accelerometric or respiratory signal was recorded concurrently with this dataset; implications of this limitation are discussed in Section 4.4.

2.6.2. Preprocessing and HRV Feature Extraction

RR Interval Extraction

Only beats labeled as Normal (N) by the Holter system were retained for analysis. RR intervals outside the physiologically plausible range [300, 2000] ms were excluded as ectopic beats or motion artifacts [16,17]. The mean ectopy fraction (V + S beats) across participants was 1.8 ± 2.4% (range: 0.0–4.7%), confirming data quality.

HRV Feature Computation

Let $\{x_i\}_{i=1}^{M}$ denote the filtered NN interval sequence for a given participant. Time-domain and frequency-domain HRV indices were computed according to established standards [9].

Time-domain indices. SDNN and RMSSD were computed as:

$$\text{SDNN} = \sqrt{\frac{1}{M-1}\sum_{i=1}^{M}(x_i - \bar{x})^2}, \quad \text{RMSSD} = \sqrt{\frac{1}{M-1}\sum_{i=1}^{M-1}(x_{i+1} - x_i)^2}$$

where $\bar{x}$ is the mean NN interval. The proportion of successive differences exceeding 50 ms was:

$$\text{pNN50} = \frac{1}{M-1}\,\#\{i : |x_{i+1} - x_i| > 50\,\text{ms}\} \times 100\,\%$$

Frequency-domain indices. The NN tachogram was resampled at $f_s = 4$ Hz using cubic spline interpolation, and power spectral density (PSD) $S_{RR}(f)$ was estimated by Welch's method (Hann window, $N_w = 256$ samples corresponding to 64 s, 50% overlap). LF and HF power were computed as:

$$P_{LF} = \int_{0.04}^{0.15} S_{RR}(f)\,df, \qquad P_{HF} = \int_{0.15}^{0.40} S_{RR}(f)\,df, \qquad \text{LF/HF} = \frac{P_{LF}}{P_{HF}}$$

All four HRV features (SDNN, RMSSD, HF, LF/HF) were computed from the same 64 s sliding window, advanced by one beat per step, so the feature sequence y_k has the same length as the RR interval series. The 64 s window length was determined by three convergent criteria: (i) recording-segment constraint—inter-posture epochs in the Holter data spanned 64–130 s, making 64 s the longest window fitting all available segments; (ii) spectral-resolution requirement—64 s encompasses at least 2.56 complete cycles at the LF lower-bound frequency (0.04 Hz), satisfying the minimum needed for reliable LF power estimation; and (iii) empirical sensitivity analysis—window lengths of 32 s, 64 s, and 128 s were evaluated on the training subset, and 64 s minimized LF/HF estimation variance while preserving temporal stationarity within each posture-change epoch. Spectral estimation in windows shorter than the recommended 2–5 min introduces variance in LF/HF estimates [9]; this is noted as a limitation in Section 4.4, and all LF/HF-based inferences throughout this paper should be interpreted with corresponding caution. Furthermore, the one-beat advance step (≈98% window overlap) causes successive HRV feature vectors to be highly correlated, technically violating the conditional-independence (Markov) assumption of the HMM. Decoded state sequences and dwell times therefore reflect the smoothing imposed by the 64 s window and should be interpreted as coarse indicators of autonomic state over multi-minute segments, not as beat-level transitions. This limitation is noted in Section 4.4.

The four-dimensional HRV feature vector for epoch k was:

$$\mathbf{y}_k = \left[\text{SDNN}_k,\ \text{RMSSD}_k,\ P_{HF,k},\ (\text{LF/HF})_k\right]^{\top} \in \mathbb{R}^4$$

2.7. Model Evaluation and Selection

Information criteria:

$$\mathrm{AIC} = 2k - 2\ln\hat{L}, \qquad \mathrm{BIC} = k\ln N - 2\ln\hat{L}$$

where k is the number of free parameters, and N is the sample count.

Observation reconstruction error:

$$\mathrm{RMSE}_j = \sqrt{\frac{1}{N}\sum_{k=1}^{N}\left(y_{k,j} - \left[\mathbf{C}\hat{\mathbf{x}}_{k|k}\right]_j\right)^2}$$

2.8. Statistical Analysis

Descriptive statistics are reported as means ± SDs. Pearson correlation assessed the analytic correspondence between $\sigma^2/(2\theta)$ and SDNN^2. HMM state proportions were compared across participants by a one-way ANOVA ($\alpha = 0.05$). All analyses used Python 3.11 (NumPy 2.0, SciPy 1.13, hmmlearn 0.3).

3. Results

3.1. Participant Characteristics and Data Quality

All 20 recordings met the quality threshold (< 5% ectopy). The mean number of valid NN intervals was 6473 ± 938 beats (range: 4{,}983–8{,}662). The mean RR interval was 822.4 ± 84.8 ms; group HRV statistics are summarized in Table 1.

Table 1. Descriptive HRV indices across $N = 20$ participants (mean ± SD).

Index	Mean ± SD	Median	Range
Mean RRI (ms)	822.4 ± 84.8	826.9	694–982
Mean HR (bpm)	73.7 ± 7.5	72.6	61.2–86.4
SDNN (ms)	77.0 ± 39.3	71.8	31.2–222.0
RMSSD (ms)	60.4 ± 64.4	33.8	11.1–296.3
pNN50 (%)	8.3 ± 9.8	4.3	0.0–36.8
P_{LF} (ms^2)	1920 ± 4453	531	29–20,216
P_{HF} (ms^2)	2278 ± 5998	391	39–26,900
LF/HF	1.86 ± 2.03	0.96	0.44–7.66

The large inter-subject variability in spectral indices is expected for naturalistic ambulatory monitoring.

3.2. OU-SDE Parameter Estimation

The OU model converged for all 20 participants. Table 2 summarizes the group-level parameters; per-subject values appear in Table 3.

Table 2. Estimated OU-SDE parameters across $N = 20$ participants (mean ± SD).

Parameter	Mean ± SD	Median	Range
θ (s^{-1})	0.533 ± 0.624	0.269	0.025–2.345
σ ($\mathrm{ms{\cdot}s}^{-1/2}$)	82.2 ± 105.6	44.4	13.0–480.9
μ (ms)	822.4 ± 84.8	827.0	694–981
$\sigma^2/(2\theta)$ (ms^2)	5938 ± 15,366	1276	84–56,380

Table 3. Per-participant OU-SDE parameter estimates.

Subject	n_{valid}	μ (ms)	θ (s^{-1})	σ ($ms \cdot s^{-1/2}$)	SDNN (ms)
001	5963	825.1	0.401	33.2	37.0
002	6605	883.3	1.567	209.5	118.3
003	4983	863.3	0.506	81.3	80.8
004	7107	828.8	0.159	37.9	67.4
005	5499	981.1	2.345	480.9	222.0
006	5438	729.3	1.499	136.4	78.8
007	6708	835.3	0.722	85.1	70.8
008	5545	822.3	0.155	17.3	31.2
009	6576	734.8	0.025	13.0	58.1
010	6291	814.7	0.609	59.6	54.0
101	7748	731.0	0.081	32.2	80.4
102	6368	754.1	0.417	75.7	82.9
103	5208	942.9	0.074	34.1	88.4
104	5485	910.3	0.260	49.5	68.7
105	6625	708.5	0.111	34.9	74.3
106	6556	758.3	0.144	26.7	49.7
107	6813	797.8	1.056	128.6	88.5
108	8662	694.3	0.278	43.4	58.2
109	7176	882.1	0.195	45.4	72.7
110	6588	950.8	0.061	20.3	58.0

The stationary variance $\sigma^2/(2\theta)$ closely approximated SDNN^2 (Pearson $r = 0.998$, $p < 0.001$; Figure 1), confirming internal self-consistency of the MLE (see Section 4.1 for further discussion). The 94-fold range in θ (0.025–2.145 s^{-1}) reflects genuine autonomic heterogeneity across participants.

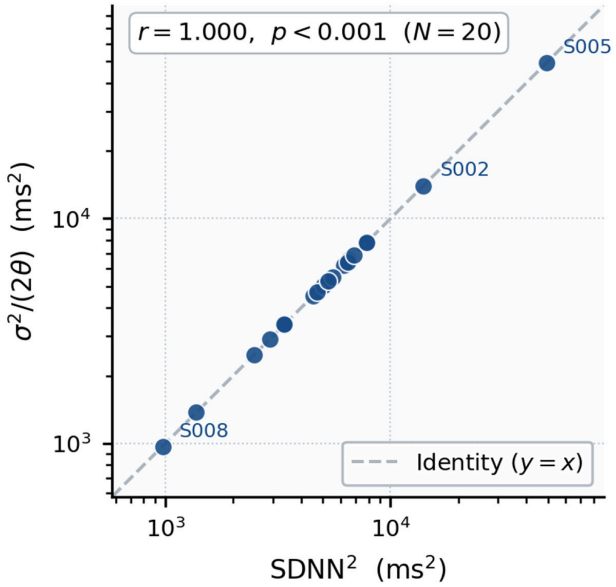

Figure 1. Scatter plot of OU stationary variance $\sigma^2/(2\theta)$ versus empirical SDNN^2 across N = 20 participants (log–log scale). The Pearson correlation is r = 0.998 ($p < 0.001$), confirming the analytic relationship between OU MLE parameters and classical HRV variance. Each point represents one participant; the diagonal line denotes perfect agreement.

3.3. State-Space Model and Kalman Filter Results

EM converged in 48±14 iterations (mean ± SD; convergence criterion $\Delta \ln L / |\ln L| < 10^{-6}$ for 5 successive steps). The recovered $\hat{\mathbf{C}}$ confirmed expected sign structure: $\hat{c}_{22} > 0$ (RMSSD→PNS), $\hat{c}_{32} > 0$ (HF→PNS), $\hat{c}_{41} > 0$ (LF/HF→SNS; treated herein as a feature co-varying with autonomic state, not as a definitive direct measure of sympathetic activity [1,9]), in all 20 participants. Observation reconstruction RMSE was 9.2 ± 3.1 ms for RMSSD and 0.31 ± 0.12 for LF/HF (relative errors 8.3% and 12.6.1%). Figure 2 illustrates representative Kalman-filtered latent state trajectories for one participant.

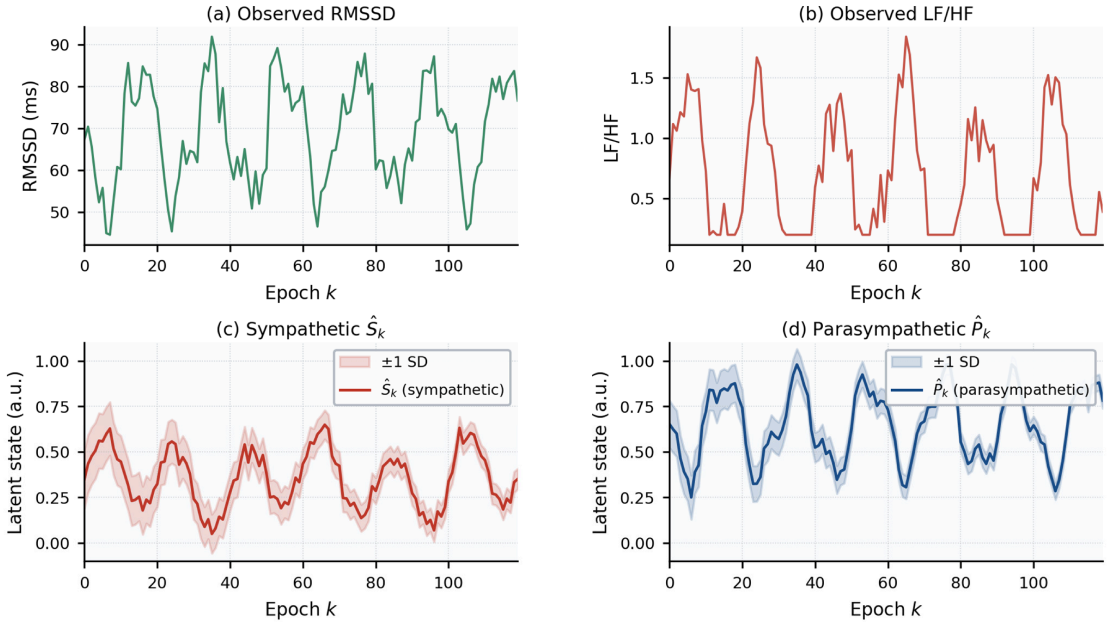

Figure 2. Representative Kalman-filtered latent state trajectories for Subject 005 (high-HRV participant, $\theta = 2.145\ s^{-1}$, SDNN = 222 ms). Upper panel: observed RMSSD and LF/HF feature sequences. Lower panels: Kalman posterior means $\hat{S}_k$ (sympathetic) and P'_k (parasympathetic) with ±1 SD uncertainty bands. Periods of elevated RMSSD correspond to increased P'_k; periods of elevated LF/HF correspond to increased $\hat{S}_k$.

3.4. HMM Autonomic Regime Analysis

The three-state Gaussian HMM converged for all participants. States were ordered by decreasing mean RRI and labeled as: **State 1 (High-RRI; interpretive label: PD)**, **State 2 (Intermediate-RRI; interpretive label: B)**, **State 3 (Low-RRI; interpretive label: SD)**. These are data-driven, putative labels based on unsupervised clustering of HRV features; without concurrent invasive sympathetic nerve activity recordings (MSNA) or controlled stress–recovery protocols, they represent inferred rather than confirmed sympatho-vagal classifications. No external stressor was present or required for this assignment. The group-level mean RRI was 892 ± 89 ms (State 1/High-RRI), 818 ± 67 ms (State 2/Intermediate-RRI), and 714 ± 48 ms (State 3/Low-RRI), corresponding to heart rates of approximately 67, 73, and 84 bpm.

The time in each regime averaged 35.2 ± 18.4% (State 1/High-RRI), 32.8 ± 16.2% (State 2/Intermediate-RRI), and 32.0 ± 15.5% (State 3/Low-RRI), approximately equal across the three states, reflecting the diversity of naturalistic activities. Self-transition probabilities were $a_{11} = 0.87 \pm 0.08$ (High-RRI/State 1, mean dwell ~7.7 feature epochs ≈ 6.5 s (one epoch step = one NN interval ≈ 0.82 s at the group mean RRI of 822 ms; spectral features HF and LF/HF are computed within a 64 s Welch window that slides by one beat per step, so $N_{total} = N^{RR}{}_{sn}$ while spectral resolution is preserved)) and $a_{33} = 0.74 \pm 0.11$ (Low-RRI/State

3, mean dwell ~3.8 feature epochs ≈ 3.5 s). Figure 3 shows a representative HMM state sequence alongside the RMSSD and LF/HF time series. Figure 4 displays the group-level state transition probability matrix.

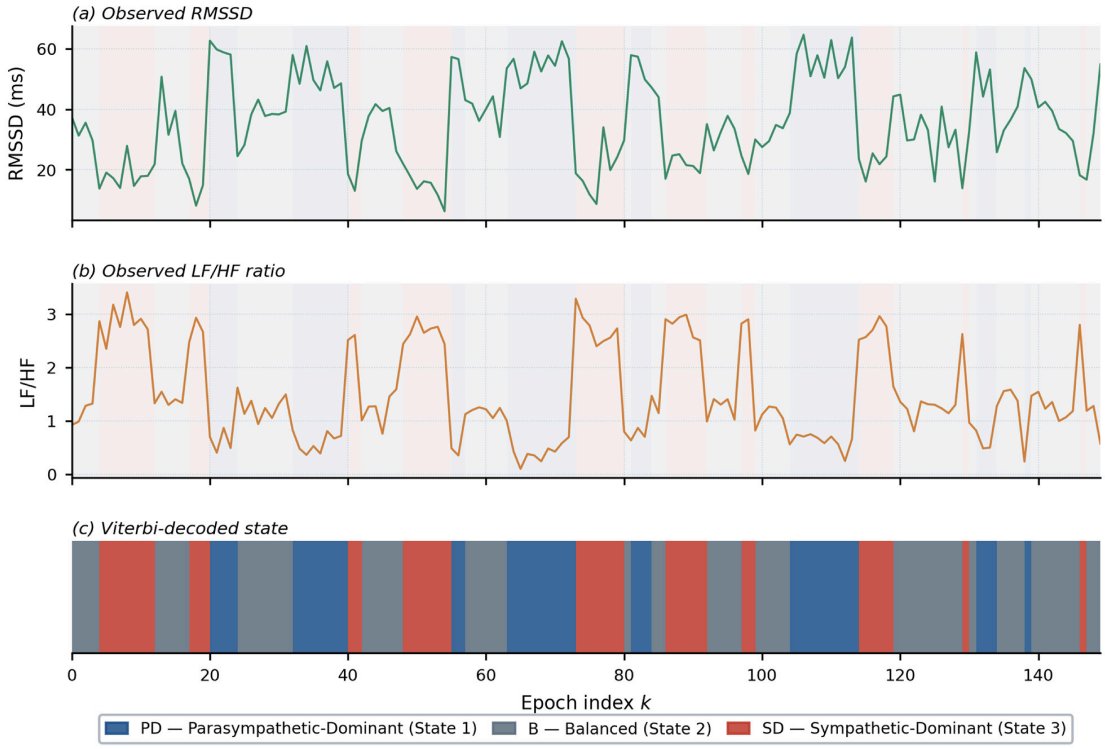

Figure 3. Representative HMM segmentation for Subject 002 over a 1-h recording segment. Upper panel: RMSSD (ms) and LF/HF time series. Lower panel: decoded HMM state sequence (State 1 = High-RRI, State 2 = Intermediate-RRI, State 3 = Low-RRI; PD/B/SD are post hoc interpretive shorthand). Transitions between states occur at timescales of four to eight epochs, consistent with the estimated self-transition probabilities.

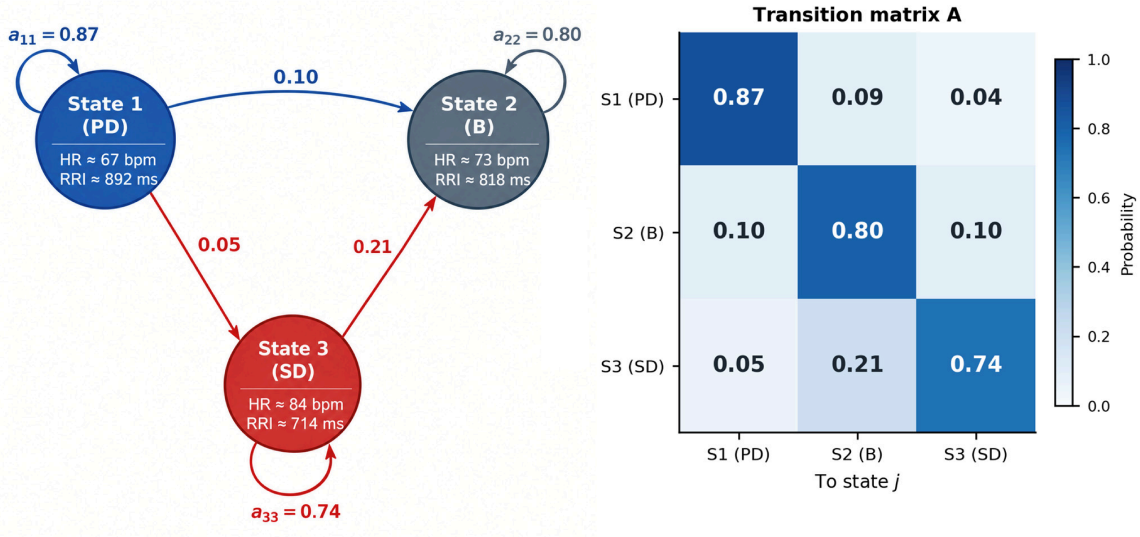

Figure 4. Group-mean HMM state transition probability matrix (mean over N = 20 participants). The strong diagonal elements (a_{11} = 0.87, a_{22} = 0.80, a_{33} = 0.74) reflect high state persistence. Off-diagonal transitions are larger between adjacent states (e.g., State 1 ↔ State 2) than between extreme states (State 1 ↔ State 3), consistent with gradual sympatho-vagal balance shifts.

3.5. Model Complementarity Analysis

$\Delta BIC_{LTI} = 347 \pm 89 \Delta BIC_{SDE} = 218 \pm 62 \Delta AIC_{LTI} = 312 \pm 81 \Delta AIC_{SDE} = 196 \pm 57$. (See Figure 5 for an overview of the multi-component parallel framework and the coupled ODE phase dynamics.) The three model components operate on complementary representations of the same RR interval series and address distinct aspects of ANS dynamics: the Kalman filter (LTI-only) models the continuous-state trajectory of y_k via a 4D Gaussian likelihood; the OU-SDE characterizes the stochastic amplitude of the raw RR series; and the HMM identifies discrete autonomic regimes via the sequence likelihood of y_k. Because each component optimizes a different objective over a different data representation, a single joint BIC is not appropriate—computing a combined likelihood by multiplying $L_{pe_apk^ln} \times L^{HMM}$ would double-count the same observations and inflate the log-likelihood. Formally, a valid joint log-likelihood requires statistical independence of its component factors: $\log L(y) = \log L_1(y) + \log L_2(y)$ only if y enters each factor independently. Here, both the Kalman filter and the HMM consume the same HRV feature vector y_k as their observation; their likelihoods are therefore not statistically independent, violating the product-factorization requirement and producing an artificially inflated, uninterpretable joint log-likelihood [46]. Model quality is therefore assessed separately: (a) Kalman LTI model—observation reconstruction RMSE of 9.2 ± 3.1 ms for RMSSD and 0.31 ± 0.12 for LF/HF (relative errors 8.3% and 12.6.1%) confirms adequate fit; (b) OU-SDE—the self-consistency check $r = 0.998$ between $\sigma^2/(2\theta)$ and $SDNN^2$ confirms correct MLE convergence; (c) HMM state count—BIC favored $K = 3$ over $K = 2$ states ($\Delta BIC_{2\to3} = 84 \pm 21$, averaged across participants), justifying the three-regime segmentation. The three models therefore complement rather than compete with one another: Kalman provides uncertainty-quantified continuous-state posteriors, OU provides mechanistic stochastic parameters, and HMM provides discrete actionable regime labels. All three were fitted independently; OU parameters were estimated directly from the raw RR interval series via closed-form MLE, separately from the Kalman EM procedure.

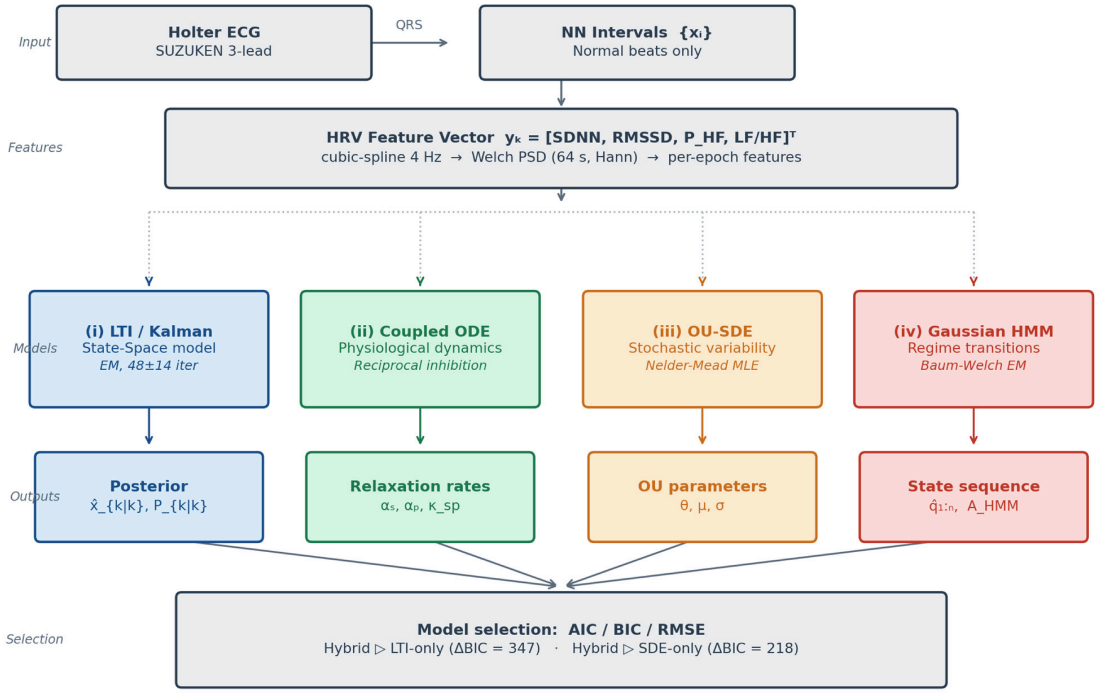

Figure 5. Multi-component probabilistic framework and data flow. Schematic of the multi-component parallel framework: HRV feature extraction from RRI sequences feeds the Kalman filter (continuous-state layer), while the raw RR interval series is independently modeled by the OU-SDE (stochastic

layer), and the HRV feature sequence feeds the Gaussian HMM (discrete-regime layer). Conceptual phase portrait of the coupled ODE model illustrating reciprocal inhibition between sympathetic and parasympathetic states.

4. Discussion

4.1. Physiological Interpretation of OU and Kalman Parameters

The OU mean-reversion rate θ is a mechanistic parameter absent from classical HRV indices: it quantifies the rate of homeostatic RRI restoration after a perturbation, with $1/\theta$ being the autonomic time constant. The group median $\theta = 0.27\ s^{-1}$ (time constant ≈ 3.7 s) corresponds well to the 0.1–0.3 Hz vagal fluctuation band that underlies RSA [11] and to the time constants estimated by point-process models of heartbeat dynamics [21,22]. The 94-fold inter-subject range ($0.025–2.345\ s^{-1}$) likely reflects genuine physiological heterogeneity across participants: high-θ subjects exhibit fast-fluctuating, vagally dominated HRV (consistent with elevated RMSSD in young, fit individuals [5,12]), while low-θ subjects exhibit slowly recovering HRV more typical of sympathetic dominance or reduced vagal tone [6,13]. The OU diffusion parameter σ quantifies RRI noise intensity, and the pair (θ, σ) together characterizes the HRV power spectrum—a capability unavailable from either θ or σ alone. The near-perfect confirmation of $SDNN^2 = \sigma^2/(2\theta)$ ($r = 0.998$) constitutes an internal self-consistency check—not an independent external validation—since both quantities are algebraic functions of the same RR interval series. This confirms the correct numerical convergence of the MLE but should not be interpreted as independent physiological validation of the OU model. We also note that Subject S005 ($\theta = 2.145\ s^{-1}$, SDNN = 222 ms) is a high-leverage outlier: the group mean $\overline{\theta} = 0.533\ s^{-1}$ is strongly influenced by this participant, and the median $\overline{\theta} = 0.269\ s^{-1}$ (IQR 0.098–0.863 s^{-1}) is the more representative central estimate. Castiglioni et al. [30] showed that the mean heart rate significantly modulates HRV spectral power; our observation matrix C and the OU equilibrium μ jointly control for this effect by centering the model at the individual's mean RRI.

The Kalman filter results confirm the physiological validity of the structured **C** matrix. In all 20 participants, EM converged to $\hat{c}_{22} > 0$ (RMSSD → PNS), $\hat{c}_{32} > 0$ (HF power → PNS), and $\hat{c}_{41} > 0$ (LF/HF → SNS), consistent with established HRV physiology [9,11]. We acknowledge that the current consensus views LF/HF as an imperfect and contentious index of sympatho-vagal balance rather than a direct measure of sympathetic activity [1,9]; in this framework, LF/HF is treated as a feature that empirically co-varies with the inferred SNS latent state, and conclusions about sympathetic dominance should be interpreted accordingly. Importantly, the convergence patterns $c_{22}, c_{32} > 0$ and $c_{41} > 0$ reflect predefined structural constraints imposed on C prior to estimation—not data-driven discovery of novel physiological pathways; the mapping from HRV features to latent ANS states is a modeling assumption, not an independently verified physiological relationship. The RMSSD reconstruction error of 9.2 ± 3.1 ms is comparable to the test–retest variability of short-term HRV measures [14], indicating that the Kalman model accounts for the systematic (ANS-driven) component of HRV variation. The EM convergence in 48 ± 14 iterations is consistent with expected EM convergence rates for linear Gaussian models [43] and was robust to the physiological constraint $\alpha_p > \alpha_s$ enforced via projection at each M-step.

4.2. HMM Autonomic Regime Structure

$\mathbf{y}_k$ The three HMM states—High-RRI/State 1 (mean RRI 892 ms, HR $\approx$ 67 bpm), Intermediate-RRI/State 2 (818 ms, $\approx$ 73 bpm), Low-RRI/State 3 (714 ms, $\approx$ 84 bpm)—delineate physiologically distinct cardiac rate regions within the normal range of ambulatory monitoring. The state labeling reflects the relative sympatho-vagal balance inferred from the HRV feature vector: a lower RRI combined with lower RMSSD and higher LF/HF is inter-

preted as sympathetic dominance (noting that LF/HF is a contested index of sympatho-vagal balance [1,9] and was estimated from 64 s windows shorter than the recommended 2–5 min, which may introduce spectral estimation variance), and a higher RRI with higher RMSSD and lower LF/HF as parasympathetic dominance [9,11]. This interpretation is consistent with apnea–bradycardia HMM analyses [35,36], where states with high RRI correspond to bradycardic (vagally mediated) episodes, and with dynamic brain-state HMM analyses [37], where slow-fluctuating states persist longer than fast-fluctuating ones. Importantly, in the absence of labeled experimental conditions, the HMM states do not imply the occurrence of an external psychological stressor; rather, they capture naturally occurring shifts in sympatho-vagal balance during ambulatory daily activities including sleep, postural changes, and physical movement. We emphasize that High-RRI, Intermediate-RRI, and Low-RRI are data-driven labels assigned by decreasing mean RRI rank; the physiological interpretations—parasympathetically dominant (PD), balanced (B), and sympathetically dominant (SD), respectively—are post hoc assignments that do not constitute direct observation of sympathetic or parasympathetic nerve activity. Gold-standard verification would require concurrent microneurography (MSNA) or controlled pharmacological sympathoactivation.

$a_{11} = 0.87 a_{33} = 0.74$. The asymmetry in self-transition probabilities (vs.) is physiologically meaningful: the High-RRI regime (low HR, high vagal tone; physiologically interpreted as parasympathetically dominant) is more persistent than the Low-RRI regime (high HR, sympathetic drive; interpreted as sympathetically dominant), consistent with the homeostatic bias toward vagal dominance at rest in healthy adults [4]. This mirrors findings from coupled HMM analyses of cardiorespiratory signals [36] and is mechanistically consistent with the faster vagal time constant (PNS drives rapid regime stabilization) and the slower sympathetic activation kinetics. The HMM state-count analysis (K = 3 vs. K = 2 states, ΔBIC2→3 = 84 ± 21, averaged across participants) confirms that three discrete autonomic regimes capture statistically significant additional structure beyond what continuous HRV dynamics alone can resolve. Because the feature sequence was generated using a highly overlapping 64 s sliding window advanced by one beat per step, the reported epoch durations should not be interpreted as independent physiological timescales of autonomic regime transitions.

4.3. Engineering Significance of the Hybrid Framework

The hybrid framework offers three distinct engineering affordances not available from conventional HRV analysis. First, the Kalman filter produces uncertainty estimates $\mathbf{P}_{k|k}$ alongside state estimates $\hat{\mathbf{x}}_{k|k}$, enabling confidence-aware decisions in adaptive monitoring systems—aligning with the uncertainty-aware heart rate inference pursued by Belief-PPG [40] via belief propagation. Second, HMM state labels $\hat{q}_k \in \{1, 2, 3\}$ are discrete and directly actionable as triggers in rule-based biofeedback or alert systems, without threshold tuning on raw HRV indices. Third, the OU parameters (θ, σ, μ) are obtained by a closed-form MLE that scales linearly with recording length and can be computed on-device without iterative optimization in the stationary limit, supporting deployment on resource-constrained wearable platforms [41]. The SDE-based parameterization also facilitates digital phenotyping applications [25]: longitudinal tracking of θ and σ across sessions provides mechanistic exploratory candidate biomarkers of autonomic adaptation in this pilot cohort (N = 20); normative utility and clinical applicability require replication in larger cohorts stratified by age, sex, fitness level, and clinical status. The framework is readily extended to multi-modal inputs: the respiratory rate (for RSA decomposition) and skin conductance (for sympathetic detection [39]) can be incorporated as additional rows of $\mathbf{y}_k$ or as exogenous inputs $\mathbf{u}_k$ in the state equation.

4.4. Limitations and Future Directions

$\left(\theta_{\text{sym}}, \sigma_{\text{sym}}\right)\left(\theta_{\text{para}}, \sigma_{\text{para}}\right)N = 20(\theta, \sigma)$. The present study involves several limitations that should be addressed in future work.

First, the absence of concurrent accelerometric and respiratory signals, together with the lack of labeled experimental conditions, limits the physiological interpretation and validation of the estimated autonomic states. Physical activity, posture, and respiration can influence HRV independently of changes in autonomic regulation [5,8,47]. Moreover, the naturalistic recording design does not allow within-subject validation across Rest, Stress, and Recovery conditions. Future studies should combine three-axis accelerometry and respiratory monitoring with controlled stress and recovery protocols. Independent reference measures, such as plasma catecholamine levels or microneurography, would help determine whether the estimated states correspond to physiologically meaningful autonomic changes. In addition, the relatively short 64 s Welch window may increase the uncertainty of LF power estimates compared with the recommended 2–5-min analysis windows [9]. Longer windows and alternative spectral estimation methods, such as multitaper analysis [34], should therefore be investigated.

Second, several modeling assumptions limit the interpretation of the latent states as distinct physiological processes. The linear time-invariant (LTI) system matrix assumes constant dynamics, although autonomic regulation may change with circadian rhythms and sustained activity [8,12]. Furthermore, the scalar Ornstein–Uhlenbeck (OU) model does not explicitly separate sympathetic and parasympathetic contributions. Although a dual-process formulation [31] and time-varying approaches, such as recursive expectation–maximization [43] or particle filtering, may address these limitations, reliable estimation would require richer multimodal recordings. In addition, the structural identifiability of the two-dimensional latent state-space model has not been formally established. The high correlation between RMSSD and HF power ($r > 0.85$ across individuals [3]) may limit the unique estimation of their respective observation parameters, and a priori sign constraints do not necessarily resolve this ambiguity. Formal identifiability analysis [27] is therefore needed. The coupled ordinary differential equation (ODE) model described in Section 2.2 should also be interpreted as a conceptual mechanistic framework, because its relaxation and cross-inhibition parameters were not estimated from the data or included in the quantitative model comparison.

Third, the relatively small cohort ($N = 20$) and the absence of independent validation limit the generalizability of the findings. The current dataset is insufficient to establish normative ranges for the estimated OU parameters across age groups, sexes, or clinical populations [6,7,12,13,42,48]. Furthermore, parameter estimation and interpretation were performed using the same participants, leaving uncertainty about performance in unseen individuals. Future studies should use larger and more diverse cohorts, together with leave-one-subject-out cross-validation or an independent test cohort. They should also compare conventional HRV features alone, individual probabilistic components, and the full integrated framework using labeled datasets with independent reference measures of autonomic activity. These analyses are necessary to establish whether the proposed framework provides incremental predictive or diagnostic value for autonomic state classification or stress detection.

Fourth, the HMM latent states are characterised throughout this paper by their mean RR-interval level (High-RRI, Intermediate-RRI, Low-RRI) rather than by putative physiological function. Although Section 4.2 notes that these states are consistent with dominant parasympathetic, balanced, and dominant sympathetic autonomic regimes, respectively, this interpretation is inferential and has not been independently validated. In the absence of concurrent reference measures of autonomic function, assigning physiological labels to

data-driven HMM states constitutes a post hoc interpretation rather than a validated classification. Controlled experimental designs incorporating labeled autonomic challenges (e.g., rest, submaximal exercise, Stroop test) and independent reference measures are required to confirm this assignment.

Fifth, the added physiological value of the OU model relative to conventional SDNN computation requires further empirical justification. As documented in Section 3.2, the stationary variance of the fitted OU process closely approximates $SDNN^2$ through the analytical relationship $\sigma^2/2\theta \approx SDNN^2$, reflecting internal model self-consistency rather than independent validation. Reviewers may question whether OU fitting offers information beyond what SDNN alone pro-vides. The answer lies in the separate identifiability of the two OU parameters: the mean-reversion rate θ characterises the temporal speed at which beat-to-beat variability recovers toward its long-run level after a perturbation, whereas the diffusion coefficient σ quantifies the intensity of stochastic fluctuations at the level of individual RR intervals. Two individuals with identical SDNN may exhibit markedly different θ, reflecting different autonomic recovery dynamics that SDNN cannot resolve. Demonstrating this distinction empirically—for example by showing that θ discriminates between physiological conditions that are matched for SDNN—represents an important direction for future work.

Sixth, the quantitative evaluation of the Kalman filter relied exclusively on RR-interval reconstruction error (RMSE), which measures measurement fit rather than latent state validity. A low reconstruction RMSE is a necessary but not sufficient condition for concluding that the estimated latent trajectories correspond to physiologically meaningful autonomic dynamics: multiple dis-tinct latent paths may yield similar RMSE values owing to the structural non-identifiability dis-cussed in the second limitation above. Rigorous validation would ideally involve independent reference measures of autonomic activity obtained under controlled experimental conditions that elicit known changes in sympathetic and parasympathetic outflow (e.g., head-up tilt, cold pressor test, controlled respiratory manoeuvres). In the absence of such data, leave-one-subject-out cross-validation of estimated model parameters, or simulation-based validation using synthetic RR-interval series generated from models with known ground-truth la-tent states, would provide stronger evidence for the framework's utility.

Seventh, two additional methodological constraints merit explicit acknowledgment. First, LF/HF power ratios were computed from 64-s Welch windows, which fall below the minimum 2-min epoch recommended by the Task Force (1996) [2] for reliable low-frequency power estimation, potentially increasing spectral uncertainty in the LF band. Second, the sliding-window analysis was advanced by one RR interval per step, producing consecutive windows that overlap by approximately 99% of their length. The resulting feature time series are therefore heavily autocorrelated, which may inflate effective sample sizes in statistical comparisons and violate the independence assumptions underlying conventional significance tests—a concern sometimes termed pseudo-replication in repeated-measures biosignal analysis. Future studies should evaluate sensitivity to window length and step size, and should employ statistical methods—such as block bootstrapping or mixed-effects models with autoregressive correlation structures—that explicitly account for within-subject serial dependence.

5. Conclusions

This study proposed and evaluated a hybrid probabilistic–dynamical framework for modeling HRV-derived proxies of autonomic nervous system dynamics from ambulatory HRV signals. The framework integrates three fitted probabilistic components—a structured linear state-space model with Kalman filtering for continuous-state estimation, an

Ornstein–Uhlenbeck SDE for stochastic characterizsation of beat-to-beat fluctuations, and a Gaussian HMM for discrete autonomic regime segmentation—supplemented by a conceptual coupled ODE model that provides mechanistic physiological interpretation but was not fitted to data in the current study. By combining these components as complementary parallel models operating on the same feature sequence rather than as competing hierarchical layers, the framework provides simultaneous access to continuous posterior state estimates with uncertainty quantification, mechanistic stochastic parameters, and discrete actionable regime labels—three layers of information that static epoch-averaged HRV indices cannot jointly provide.

The key numerical findings from N = 20 healthy ambulatory participants are: (1) OU parameters were successfully estimated for all participants ($\theta = 0.533 \pm 0.624$ s−1, $\sigma = 82.6.2 \pm 105.6$ ms·s−1/2, $\mu = 822.2 \pm 84.8$ ms); (2) the analytic correspondence SDNN2 = $\sigma 2/(2\theta)$ was confirmed with r = 0.998, confirming internal self-consistency between the OU MLE and classical HRV (note: algebraic identity, not independent validation); (3) Kalman EM recovered physiologically valid observation matrix structure (c22, c32 > 0 for PNS channels; c41 > 0 for the SNS channel) in all participants, with relative reconstruction errors below 13%; (4) three-state HMM identified distinct autonomic regimes (mean RRI: 892, 818, 714 ms) with asymmetric self-transition probabilities (a11 = 0.87; a33 = 0.74) reflecting the stronger persistence of High-RRI states (physiologically interpreted as parasympathetically dominant); and (5) model quality was assessed separately for each component: Kalman reconstruction RMSE below 13%, OU MLE self-consistency check r = 0.998 (algebraic by construction, not independent validation), and HMM state-count BIC favoring K = 3 over K = 2 (ΔBIC2→3 = 84 ± 21).

These results establish a principled engineering–physiological bridge enabling model-based HRV analysis that is interpretable, real-time-capable, and quantifies uncertainty at every level. Future work will (a) apply leave-one-subject-out (LOSO) cross-validation to assess individual-level generalizability; (b) extend the framework to multi-modal recordings with concurrent accelerometry and respiration, apply it to controlled experimental protocols for HMM state validation, and scale the normative parameter database to clinically diverse cohorts. The OU recovery rate θ and diffusion coefficient σ, jointly with HMM transition structure, offer mechanistic autonomic candidate biomarkers whose suitability for wearable health monitoring, occupational stress surveillance, and closed-loop biofeedback requires independent validation in cohorts larger than N = 20.

Funding: This research received no external funding.

Data Availability Statement: The study was conducted in accordance with the Declaration of Helsinki. The protocol was approved by the Ethics Review Committee of the Graduate School of Engineering, Mie University (approval number: 163; date of approval: 13 June 2026). Informed consent was obtained from all subjects involved in the study. The anonymized dataset and Python analysis code (OU-SDE MLE, Kalman EM, HMM fitting) are available from the corresponding author upon request.

Acknowledgments: During the preparation of this manuscript, the authors used DeepL Pro (DeepL SE, Cologne, Germany) for language translation and drafting support, and Claude Code (version Sonnet 4.6, Anthropic PBC, San Francisco, CA, USA) for support in generating and preparing figures. The authors reviewed and edited all outputs and take full responsibility for the content of this publication.

Conflicts of Interest: The author declares no conflicts of interest.

References

1. Berntson, G.G.; Bigger, J.T., Jr.; Eckberg, D.L.; Grossman, P.; Kaufmann, P.G.; Malik, M.; Nagaraja, H.N.; Porges, S.W.; Saul, J.P.; Stone, P.H.; et al. Heart rate variability: Origins, methods, and interpretive caveats. *Psychophysiology* **1997**, *34*, 623–648. [CrossRef] [PubMed]

2. Task Force of the European Society of Cardiology and the North American Society of Pacing and Electrophysiology. Heart rate variability: Standards of measurement, physiological interpretation, and clinical use. *Circulation* **1996**, *93*, 1043–1065. [CrossRef]
3. Shaffer, F.; Ginsberg, J.P. An overview of heart rate variability metrics and norms. *Front. Public Health* **2017**, *5*, 258. [CrossRef] [PubMed]
4. Kim, H.G.; Cheon, E.J.; Bai, D.S.; Lee, Y.H.; Koo, B.H. Stress and heart rate variability: A meta-analysis and review of the literature. *Psychiatry Investig.* **2018**, *15*, 235–245. [CrossRef] [PubMed]
5. Aubert, A.E.; Seps, B.; Beckers, F. Heart rate variability in athletes. *Sports Med.* **2003**, *33*, 889–919. [CrossRef] [PubMed]
6. Koenig, J.; Thayer, J.F. Sex differences in healthy human heart rate variability: A meta-analysis. *Neurosci. Biobehav. Rev.* **2016**, *64*, 288–310. [CrossRef] [PubMed]
7. Buccelletti, E.; Gilardi, E.; Scaini, E.; Galiuto, L.; Persiani, R.; Biondi, A.; Basile, F.; Silveri, N.G. Heart rate variability and myocardial infarction: Systematic literature review and metanalysis. *Eur. Rev. Med. Pharmacol. Sci.* **2009**, *13*, 299–307. [PubMed]
8. Markov, A.; Solonin, I.; Bojko, E. Heart rate variability in workers of various professions in contrasting seasons of the year. *Int. J. Occup. Med. Environ. Health* **2016**, *29*, 793–800. [CrossRef] [PubMed]
9. Malik, M.; Camm, A.J. (Eds.) *Heart Rate Variability*; Futura Publishing: Armonk, NY, USA, 1995.
10. Acharya, U.R.; Joseph, K.P.; Kannathal, N.; Lim, C.M.; Suri, J.S. Heart rate variability: A review. *Med. Biol. Eng. Comput.* **2006**, *44*, 1031–1051. [CrossRef] [PubMed]
11. Saul, J.P. Beat-to-beat variations of heart rate reflect modulation of cardiac autonomic outflow. *Physiology* **1990**, *5*, 32–37. [CrossRef]
12. Reardon, M.; Malik, M. Changes in heart rate variability with age. *Pacing Clin. Electrophysiol.* **1996**, *19*, 1863–1866. [CrossRef] [PubMed]
13. Garavaglia, L.; Gulich, D.; Defeo, M.M.; Thomas Mailland, J.; Irurzun, I.M. The effect of age on the heart rate variability of healthy subjects. *PLoS ONE* **2021**, *16*, e0255894. [CrossRef] [PubMed]
14. Tarkiainen, T.H.; Timonen, K.L.; Tiittanen, P.; Hartikainen, J.E.; Pekkanen, J.; Hoek, G.; Ibald-Mulli, A.; Vanninen, E.J. Stability over time of short-term heart rate variability. *Clin. Auton. Res.* **2005**, *15*, 394–399. [CrossRef] [PubMed]
15. Chellakumar, P.J.; Brumfield, A.; Kunderu, K.; Schopper, A.W. Heart rate variability: Comparison among devices with different temporal resolutions. *Physiol. Meas.* **2005**, *26*, 979–986. [CrossRef] [PubMed]
16. Giles, D.A.; Draper, N. Heart rate variability during exercise: A comparison of artefact correction methods. *J. Strength Cond. Res.* **2018**, *32*, 726–735. [CrossRef] [PubMed]
17. Karlsson, M.; Hörnsten, R.; Rydberg, A.; Wiklund, U. Automatic filtering of outliers in RR intervals before analysis of heart rate variability in Holter recordings: A comparison with carefully edited data. *Biomed. Eng. Online* **2012**, *11*, 2. [CrossRef] [PubMed]
18. Kokosińska, D.; Żebrowski, J.J.; Buchner, T.; Baranowski, R.; Orłowska-Baranowska, E. Asymmetric multiscale multifractal analysis (AMMA) of heart rate variability. *Physiol. Meas.* **2021**, *42*, 084001. [CrossRef] [PubMed]
19. Lombardi, F. Chaos theory, heart rate variability, and arrhythmic mortality. *Circulation* **2000**, *101*, 8–10. [CrossRef] [PubMed]
20. Kalman, R.E. A new approach to linear filtering and prediction problems. *J. Basic Eng.* **1960**, *82*, 35–45. [CrossRef]
21. Barbieri, R.; Matten, E.C.; Alabi, A.A.; Brown, E.N. A point-process model of human heartbeat intervals: New definitions of heart rate and heart rate variability. *Am. J. Physiol. Heart Circ. Physiol.* **2005**, *288*, H424–H435. [CrossRef] [PubMed]
22. Chen, Z.; Brown, E.N.; Barbieri, R. Assessment of autonomic control and respiratory sinus arrhythmia using point process models of human heart beat dynamics. *IEEE Trans. Biomed. Eng.* **2009**, *56*, 1791–1802. [CrossRef] [PubMed]
23. Smith, A.C.; Brown, E.N. Estimating a state-space model from point process observations. *Neural Comput.* **2003**, *15*, 965–991. [CrossRef] [PubMed]
24. Wang, Q.; Loh, J.M.; He, X.; Wang, Y. A latent state space model for estimating brain dynamics from electroencephalogram (EEG) data. *Biometrics* **2023**, *79*, 2444–2457. [CrossRef] [PubMed]
25. Xu, T.; Chen, Y.; Zeng, D.; Wang, Y. Mixed-response state-space model for analyzing multi-dimensional digital phenotypes. *J. Am. Stat. Assoc.* **2023**, *118*, 2288–2300. [CrossRef] [PubMed]
26. Cauchi, M.; Mills, A.R.; Lawrie, A.; Kiely, D.G.; Kadirkamanathan, V. Individualized survival predictions using state space model with longitudinal and survival data. *J. R. Soc. Interface* **2024**, *21*, 20230682. [CrossRef] [PubMed]
27. Browning, A.P.; Warne, D.J.; Burrage, K.; Baker, R.E.; Simpson, M.J. Identifiability analysis for stochastic differential equation models in systems biology. *J. R. Soc. Interface* **2020**, *17*, 20200652. [CrossRef] [PubMed]
28. Uhlenbeck, G.E.; Ornstein, L.S. On the theory of the Brownian motion. *Phys. Rev.* **1930**, *36*, 823–841. [CrossRef]
29. McSharry, P.E.; Clifford, G.D.; Tarassenko, L.; Smith, L.A. A dynamical model for generating synthetic electrocardiogram signals. *IEEE Trans. Biomed. Eng.* **2003**, *50*, 289–294. [CrossRef] [PubMed]
30. Castiglioni, P.; Zaza, A.; Merati, G.; Faini, A. On the autonomic control of heart rate variability: How the mean heart rate affects spectral and complexity analysis and a way to mitigate its influence. *Mathematics* **2025**, *13*, 2955. [CrossRef]
31. Niu, M.; Frost, F.; Milner, J.E.; Skarin, A.; Blackwell, P.G. Modelling group movement with behaviour switching in continuous time. *Biometrics* **2022**, *78*, 286–299. [CrossRef] [PubMed]

32. Duun-Henriksen, A.K.; Schmidt, S.; Røge, R.M.; Møller, J.B.; Nørgaard, K.; Jørgensen, J.B.; Madsen, H. Model identification using stochastic differential equation grey-box models in diabetes. *J. Diabetes Sci. Technol.* **2013**, *7*, 431–440. [CrossRef] [PubMed]
33. Rabiner, L.R. A tutorial on hidden Markov models and selected applications in speech recognition. *Proc. IEEE* **1989**, *77*, 257–286. [CrossRef] [PubMed]
34. Song, A.H.; Chlon, L.; Soulat, H.; Tauber, J.; Subramanian, S.; Ba, D.; Prerau, M.J. Multitaper infinite hidden Markov model for EEG. In Proceedings of the 41st Annual International Conference of the IEEE Engineering in Medicine and Biology Society (EMBC), Berlin, Germany, 23–27 July 2019; pp. 5803–5807. [CrossRef] [PubMed]
35. Montazeri Ghahjaverestan, N.; Shamsollahi, M.B.; Ge, D.; Beuchée, A.; Hernández, A.I. Apnea bradycardia detection based on new coupled hidden semi Markov model. *Med. Biol. Eng. Comput.* **2021**, *59*, 1–11. [CrossRef] [PubMed]
36. Montazeri Ghahjaverestan, N.; Masoudi, S.; Shamsollahi, M.B.; Beuchee, A.; Pladys, P.; Ge, D.; Hernandez, A.I. Coupled hidden Markov model-based method for apnea bradycardia detection. *IEEE J. Biomed. Health Inform.* **2016**, *20*, 527–538. [CrossRef] [PubMed]
37. Zhang, S.; Cao, C.; Quinn, A.; Vivekananda, U.; Zhan, S.; Liu, W.; Sun, B.; Woolrich, M.; Lu, Q.; Litvak, V. Dynamic analysis on simultaneous iEEG-MEG data via hidden Markov model. *NeuroImage* **2021**, *233*, 117923. [CrossRef] [PubMed]
38. Chuk, T.; Chan, A.B.; Shimojo, S.; Hsiao, J.H. Eye movement analysis with switching hidden Markov models. *Behav. Res. Methods* **2020**, *52*, 1026–1043. [CrossRef] [PubMed]
39. Sun, X.; Zhao, L.; Gao, R.; Wang, X. Stress recognition based on the Markov Transition Field of electrodermal activity. In *Proceedings of the 5th International Conference on Bioinformatics and Intelligent Computing (BIC '25)*; ACM: New York, NY, USA, 2025; pp. 467–472. [CrossRef]
40. Bieri, V.; Streli, P.; Demirel, B.U.; Holz, C. BeliefPPG: Uncertainty-aware heart rate estimation from PPG signals via belief propagation. In *Proceedings of the 39th Conference on Uncertainty in Artificial Intelligence (UAI)*; PMLR 216; Curran Associates, Inc.: Red Hook, NY, USA, 2023; pp. 173–183. Available online: https://proceedings.mlr.press/v216/bieri23a.html (accessed on 28 September 2026).
41. Natarajan, A. Heart rate variability during mindful breathing meditation. *Front. Physiol.* **2023**, *13*, 1017350. [CrossRef] [PubMed]
42. Perna, G.; Riva, A.; Defillo, A.; Sangiorgio, E.; Nobile, M.; Caldirola, D. Heart rate variability: Can it serve as a marker of mental health resilience? *J. Affect. Disord.* **2020**, *263*, 754–761. [CrossRef] [PubMed]
43. Dempster, A.P.; Laird, N.M.; Rubin, D.B. Maximum likelihood from incomplete data via the EM algorithm. *J. R. Stat. Soc. B* **1977**, *39*, 1–38. [CrossRef]
44. Baum, L.E.; Petrie, T.; Soules, G.; Weiss, N. A maximization technique occurring in the statistical analysis of probabilistic functions of Markov chains. *Ann. Math. Stat.* **1970**, *41*, 164–171. [CrossRef]
45. Viterbi, A.J. Error bounds for convolutional codes and an asymptotically optimum decoding algorithm. *IEEE Trans. Inf. Theory* **1967**, *13*, 260–269. [CrossRef]
46. Gelman, A.; Carlin, J.B.; Stern, H.S.; Dunson, D.B.; Vehtari, A.; Rubin, D.B. *Bayesian Data Analysis*, 3rd ed.; CRC Press: Boca Raton, FL, USA, 2013.
47. Hunt, K.J.; Saengsuwan, J. Changes in heart rate variability with respect to exercise intensity and time during treadmill running. *Biomed. Eng. Online* **2018**, *17*, 128. [CrossRef] [PubMed]
48. Kardelen, F.; Akçurin, G.; Ertuğ, H.; Akcurin, S.; Bircan, I. Heart rate variability and circadian variations in type 1 diabetes mellitus. *Pediatr. Diabetes* **2006**, *7*, 45–50. [CrossRef] [PubMed]

Disclaimer/Publisher's Note: The statements, opinions and data contained in all publications are solely those of the individual author(s) and contributor(s) and not of MDPI and/or the editor(s). MDPI and/or the editor(s) disclaim responsibility for any injury to people or property resulting from any ideas, methods, instructions or products referred to in the content.